Sublytic gasdermin-D pores captured in atomistic molecular simulations

Stefan L. Schaefer[†] and Gerhard Hummer[*,†,‡]

[†]*Department of Theoretical Biophysics, Max-Planck-Institute of Biophysics, Max-von-Laue Str. 3, 60438 Frankfurt am Main, Germany*

[‡]*Institute of Biophysics, Goethe University Frankfurt, Max-von-Laue Str. 1, 60438 Frankfurt am Main, Germany*

E-mail: gerhard.hummer@biophys.mpg.de

Abstract

Gasdermin-D (GSDMD) is the ultimate effector of pyroptosis, a form of programmed cell death associated with pathogen invasion and inflammation. After proteolytic cleavage by caspases activated by the inflammasome, the GSDMD N-terminal domain ($GSDMD^{NT}$) assembles on the inner leaflet of the plasma membrane and induces the formation of large membrane pores. We use atomistic molecular dynamics simulations to study $GSDMD^{NT}$ monomers, oligomers, and rings in an asymmetric plasma membrane mimetic. We identify distinct interaction motifs of $GSDMD^{NT}$ with phosphatidylinositol-4,5-bisphosphate ($PI(4,5)P_2$) and phosphatidylserine (PS) headgroups and describe differential lipid binding between the pore and prepore conformations. Oligomers are stabilized by shared lipid binding sites between neighboring monomers acting akin to double-sided tape. We show that already small $GSDMD^{NT}$ oligomers form stable, water-filled and ion-conducting membrane pores bounded by curled beta-sheets. In large-scale simulations, we resolve the process of pore formation by lipid detachment from $GSDMD^{NT}$ arcs and lipid efflux from partial rings. We find that that high-order $GSDMD^{NT}$ oligomers can crack under the line tension of 86 pN created by an open membrane edge to form the slit pores or closed $GSDMD^{NT}$ rings seen in experiment. Our simulations provide a detailed view of key steps in $GSDMD^{NT}$-induced plasma membrane pore formation, including sublytic pores that explain nonselective ion flux during early pyroptosis.

Significance

Gasdermins execute pyroptotic membrane perforation that is responsible for the release of inflammatory signals and ultimately leads to lytic cell death. They assemble into an approximately 20 nm wide transmembrane β-barrel pore across the plasma membrane. With atomistic molecular simulations of gasdermin-D in a realistic asymmetric plasma membrane mimetic, we show that already small oligomers can form stable water-filled and ion-conducting pores. Simulations of larger oligomeric assemblies reveal instabilities in the cir-

cular prepore and demonstrate pathways to the formation of slit and ring-shaped pores. Our work gives structural and dynamic insight into how small membrane pores emerge that dissipate the ionic gradient of the cell, but not yet cause cell lysis.

Introduction

Pyroptosis is a recently discovered form of regulated cell death that leads to lysis of the affected cell and to the release of damage-associated molecular patterns (DAMPs) such as mature IL-1β and IL-18.[1–4] Pyroptosis is tightly regulated by the assembly of canonical or non-canonical inflammasomes and the activation or presence of certain caspases, granzymes or pathogenic proteases.[5–9] In turn, these proteases activate gasdermins by cleaving off their C-terminal domains, which exposes a basic surface on the N-terminal domain.[3,7] The N-terminal domain then binds to the plasma membrane, oligomerizes, and inserts a β-sheet into the membrane, similar to bacterial β pore-forming toxins[10] though acting from the inner leaflet. The hydrophobic face of the β-sheet anchors the sheet into the membrane and its hydrophilic face facilitates the opening of an approximately 20 nm wide membrane pore.[3,11] In addition to cytokine release, the opening of the pore in most cases leads to an osmotic shock that ultimately disrupts the integrity of the cell.[12] Gasdermins play a crucial role in the innate immune response to pathogen infection. Altered activation of pyroptosis has also been associated with various types of cancers and cancer treatments.[7,13] A detailed, molecular-level understanding of gasdermin action is thus biomedically relevant.[14]

Gasdermin-D (GSDMD) is the best-characterized gasdermin of the six human isoforms. It is expressed in many tissues, including cells of the gastrointestinal system, the circulatory system, the skin, the lung and many immune cells.[15] Its central role in infection response makes GSDMD a target of therapeutic applications.[7] After proteolytic cleavage, GSDMD N-terminal domain ($GSDMD^{NT}$) binds specifically to negatively charged lipids of the inner leaflet of the plasma membrane, where it forms β-pores comprising around 30 subunits.[3,16–19]

The exact order and mechanism with which GSDMD^{NT} binds the plasma membrane, oligomerizes, and spontaneously inserts its transmembrane β-hairpins into the membrane is not fully understood. Cryo-electron microscopy (cryo-EM) studies resolved the pore structures of mouse gasdermin-A3 (GSDMA3)[11] and human GSDMD,[3] respectively, and identified the density of a fully assembled prepore ring stacked opposite the pore structure and separated by detergent. Very recently, atomic force microscopy (AFM) imaging resolved circular assemblies that could be washed off the supported bilayer.[20] These results promote the idea that GSDMD^{NT} forms complete rings before folding and inserting its β-sheet. On the other hand, AFM experiments of growing assemblies[19] and nonselective ion influx and efflux in the early phases of pyroptosis[21,22] favor an alternative pore assembly pathway, in which GSDMD^{NT} first forms membrane-inserted arcs and slits, which can then grow over time to build full circular pores.[23]

Here, we use multi-microsecond atomistic molecular dynamics (MD) simulations to study the lipid interactions, dynamics, and structural stability of differently sized GSDMD^{NT} oligomers and rings in prepore and pore conformation. For our simulations, we use a realistic asymmetric plasma membrane mimetic. The simulations give us a detailed view of lipid binding, which is critically important to target GSDMD^{NT} to the inner leaflet of the plasma membrane and may play a role in inducing the transition from prepore to pore conformation. The simulations also allow us to watch in real time as lipids recede from membrane-inserted GSDMD^{NT} oligomers to form stable membrane pores with diameters from 1 to 20 nm. In turn, we show that the resulting membrane forces impact the formation and relative stability of GSDMD^{NT} arc, slit, and circular ring structures, as seen in experiments. We conclude by contrasting the different pore formation pathways and raising open questions.

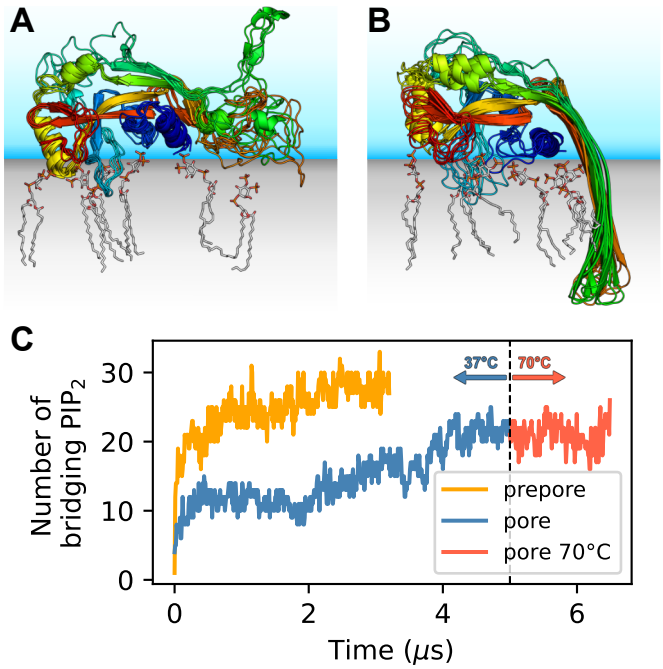

Figure 1: **GSDMD^{NT} interacts tightly with anionic lipids.** Overlay of six representative PI(4,5)P_2 bound poses of the prepore monomer (A) and the 33-mer GSDMD^{NT} ring in pore conformation (B). GSDMD^{NT} is shown in cartoon representation and colored using a rainbow spectrum from blue (N-terminus) to red (C-terminus). The β1-β2 loop is colored in cyan, the α1 helix in dark blue, the α3 helix in yellow, and the C-terminus in red. PI(4,5)P_2 is shown in grey licorice representation with orange phosphorus and red oxygen atoms. Hydrogen atoms are not shown for clarity. The membrane and solvent are schematically shown with gray and blue shades, respectively. (C) Number of PI(4,5)P_2 molecules that interact simultaneously with two subunits of the prepore (orange) and pore (blue, red) 33-mer rings. After 5 μs the pore simulation at 37°C was continued for 1.5μs at 70°C.

Results

GSDMD^{NT} binds to acidic lipids in the plasma membrane. GSDMD^{NT} strongly interacted with acidic lipids in all our simulations of the prepore and pore conformations. Distinct clusters of phosphatidylinositol-4,5-bisphosphate (PI(4,5)P_2) and phosphatidylserine (PS) lipids of the intracellular leaflet formed at the protein underside, stabilized by abundant basic amino acids (see Table S1 for a list of lipids). The following sites were occupied with high consistency. The β1-β2 loop (residues 42-55; numbering as in the cryo-EM structure[3]) emerged as a focal point of interactions with anionic lipids (Figure 1). Its aromatic residues W48, F49, W50, and Y54 anchored the loop deeply into the upper membrane

leaflet. Anionic lipids clustered at the interface of the β1-β2 loop with the α1 helix (dominated by interactions with R10, K51, R53), the α3 helix (dominated by interactions with K43, R53, K55, R153), and the disordered C-terminus (dominated by interactions with K51, K235, K236, R238). An additional binding site for anionic lipids formed between α1 and β7 was stabilized by interactions with R7, R10, R11, and R178. In around two thirds of interfaces between neighboring subunits in the 33-mer pore we find a PI(4,5)P_2 headgroup that interacts with both neighbors at the same time (Figure 1C). Due to the flexible, unfolded hairpins of the prepore 33-mer, there even more PI(4,5)P_2 interconnect two subunits.

The lipid interactions in the prepore monomer and the 33-mer pore differ in three notable aspects. (1) In the prepore monomer, the loops eventually forming the membrane spanning β-sheet in the pore conformation remained mostly unfolded and resided on the membrane surface with only few residues penetrating the interface (Figure 1A, green and orange). Their basic amino acids faced the membrane to form lipid contacts. By contrast, in the pore conformation, only R178, R174, and K204 bound PI(4,5)P_2, whereas the side chains of the other basic hairpin residues pointed towards the water-filled pore (K177, K203) or stabilized the tips of the sheet in the extracellular leaflet (K103, R183). In the pore conformation, a single PI(4,5)P_2 bound to R7, R174, and R178 simultaneously in some instances. (2) In the pore conformation, the α1 helices (Figure 1B, dark blue) formed a continuous belt lying flat on the membrane. By contrast, in the prepore monomer the α1 helix was tilted at an angle of ≈30° with respect to the membrane plane, with the N-terminus pointing towards the membrane (Figure 1A, dark blue). (3) Whereas the α3 helix (Figure 1A,B, yellow) was lifted off the membrane in the pore conformation, in the prepore monomer its C-terminal residues lay directly on the membrane interface. This created a lipid binding site between α3 around the C-terminus and residues K145, Q149, and R151, which is unique to the monomeric prepore conformation. R153 formed frequent contacts to acidic lipid headgroups in both conformations.

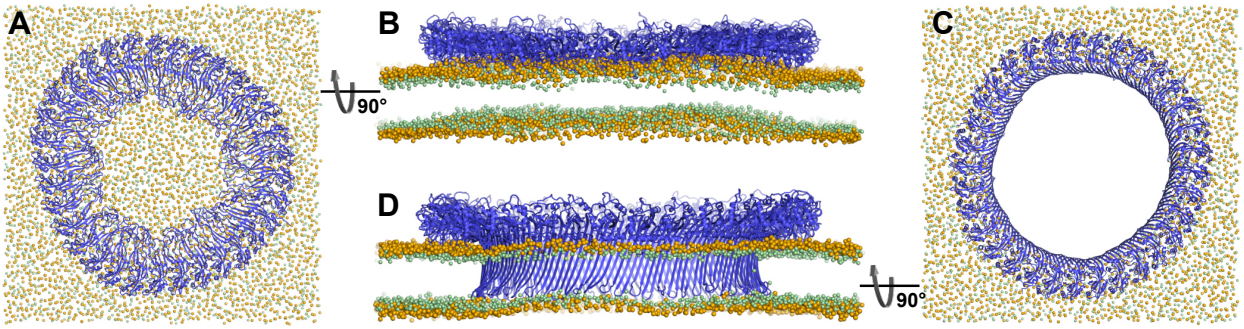

Figure 2: **Atomistic MD simulations of GSDMD^{NT} 33-mer rings in prepore and pore conformation.** Prepore (A,B; after 3.5 μs of MD) and pore rings (C,D; after 5 μs) are viewed from the top (A,C) and side (B,D). GSDMD^{NT} is shown in blue cartoon representation, lipid headgroup phosphates and glycerol oxygens are shown as orange and green spheres, respectively. Water, ions and lipid tails are not shown for clarity. The membrane under the prepore ring (A,B) is continuous but visibly bent upwards into the ring (B). In the pore conformation (C,D), lipids are absent from the central pore, which is lined by a continuous, membrane spanning β-barrel.

Prepore GSDMD^{NT} rings deform lipid membrane. To gain insight into the dynamics and stability of GSDMD^{NT} ring assemblies, we performed simulations of the full 33-mer assemblies, starting from its proposed prepore conformation and from its resolved pore conformation.[3] In the prepore conformation, the 33-mer complex maintained a nearly circular shape and remained tightly bound to the intracellular leaflet of the plasma membrane for the entirety of the 3.5 μs simulation (Figure 2A). Within the first nanoseconds of the production simulation, it deformed the membrane upwards into a crown shape (Figure 2B). To assess whether this upwards bending is affected by the limited size of the membrane, we performed another simulation of the circular prepore structure on a larger membrane (46×46 nm^2) for 2.2 μs. There, the upwards bending caused by GSDMD^{NT} was even more pronounced (Figure S1B). Noticeably, however, in this larger system, broken inter-subunit contacts between neighboring GSDMD^{NT} globular domains resulted in distortions of the ring shape (Figure S1A). It is conceivable that the local cracks in the ring were caused by the stress resulting from more pronounced membrane deformations in the system with a larger membrane patch.

GSDMD^{NT} 33-mer rings form stable membrane pores. In the pore conformation, GSDMD^{NT} stabilized a 21.6 nm wide, water-filled pore with a fully intact β-sheet lining its side (Figure 2C,D). During the entire simulation (5 μs), the membrane remained flat (Figure 2D), which is in contrast to the prepore ring. However, around the tips of the inserted hairpins the membrane was thinned because the hairpins are not long enough to reach fully across the membrane to the lipid headgroups of the extracellular leaflet. Nevertheless, the overall topology only deviated minimally from its initial perfectly circular shape and no gaps in the ring of globular domains opened up in 5 μs of MD.

Small oligomers of membrane-inserted GSDMD^{NT} create stable membrane pores. To test whether small oligomers can remain stably inserted in the membrane, we performed simulations of a membrane inserted monomer and of different-size oligomers (2, 3, 5, 8, and 10-mer), starting from arc-like segments taken out of the circular 33-mer cryo-EM structure in pore conformation.[3] Independent of the number of subunits, all GSDMD^{NT} systems, including the monomer, remained stably inserted in the membrane for the entirety of our simulations (Figure 3A-F). On the pore-facing side of the inserted β-sheet, this led to disruptions of the membrane integrity, because the hydrophilic residues on this side drew water and phospholipid headgroup moieties into the hydrophobic membrane core region. While the water chains along the small sheet of monomeric GSDMD^{NT} were regularly interrupted, all oligomeric systems maintained a continuous water column on the pore-facing side of the inserted β-sheet. Sodium and chloride ions permeated in both directions through the water-filled oligomeric pores (Figure 3G). The number of permeation events increased with oligomer size.

In systems with two or more GSDMD^{NT}, we found that the β-sheet curled up to form pores (Figure 3B-F). Whereas the edge of the sheet formed by the β3 strand stayed normal to the membrane plane, the other end of the sheet formed by the β7-β8 hairpin tilted upwards to an angle of ≈55° and almost crossed the membrane plane (Figure 3C,E front view). In the

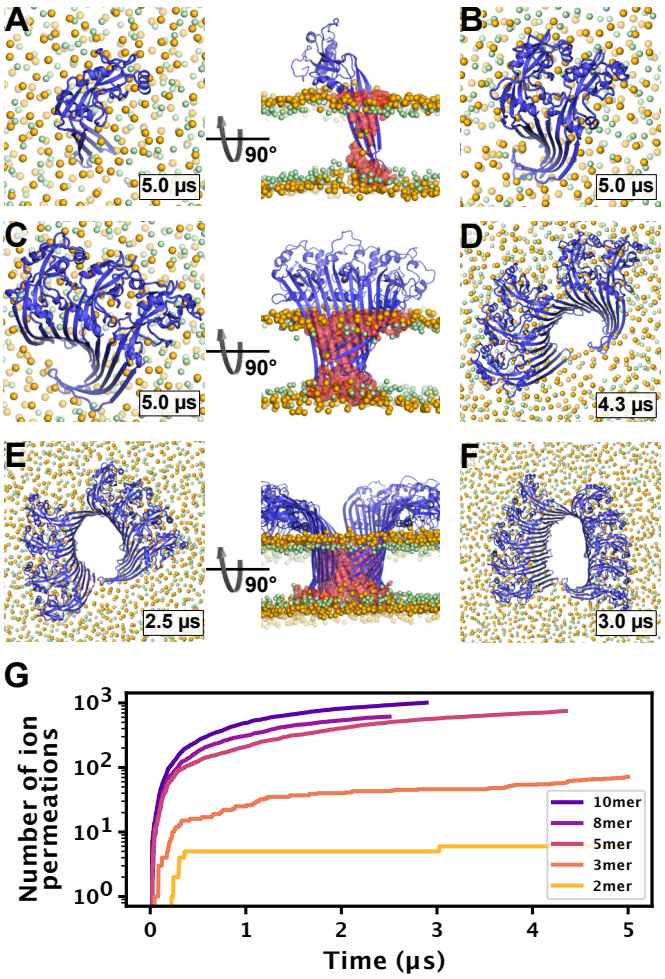

Figure 3: **MD simulations of small GSDMD^{NT} oligomers.** GSDMD^{NT} monomer (A), dimer (B), trimer (C), pentamer (D), octamer (E) and decamer (F) remain membrane inserted for the full duration of the respective MD simulations. The β-sheets of 2, 3, 5, 8, and 10-mers coil up into small membrane pores filled with water (water inside the pore shown as red volume in the right panels of A, C, E). The GSDMD^{NT} backbones are shown in blue cartoon representation. Lipid headgroup phosphates and glycerol oxygens are shown as orange and green spheres, respectively. Water, ions, and lipid tails are not shown for clarity except in the right panels of A, C, E. (G) Cumulative sodium and chloride ion permeation events during the simulations. No ions permeated the membrane in the monomer simulation.

resulting pores of oval shape, the bent β7-β8 hairpin coats one of the highly curved narrow membrane edges.

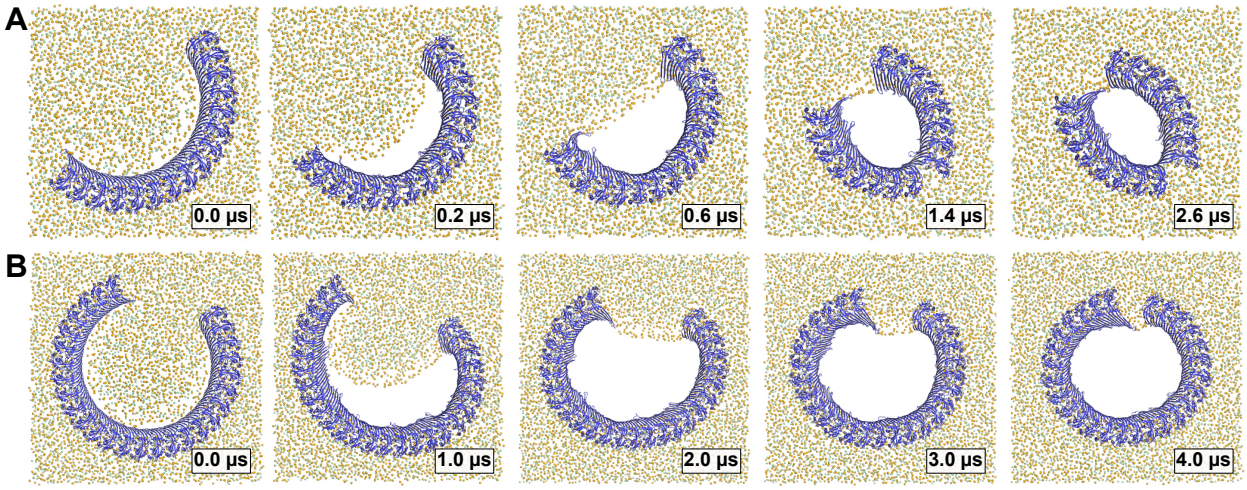

Figure 4: **Arc-shaped GSDMD^{NT} oligomers transition into slit or ring-shaped membrane pores.** Top views of GSDMD^{NT} arcs comprising 16 (A) and 27 (B) subunits in pore conformation along MD simulation trajectories (time points indicated) show phospholipid headgroups (orange spheres) and cholesterol oxygens (green spheres) receding from the inserted β-sheet, before the open protein edges approach each other and close into slit-shaped (A) or ring-shaped (B) pores. Water, ions and lipid tails are not shown for clarity.

High membrane edge tension drives the formation of slit and ring shaped pores. We also performed atomistic multi-microsecond MD simulations of larger membrane inserted oligomers with 16 and 27 GSDMD^{NT}, respectively. In the GSDMD^{NT} 16-mer and 27-mer simulations (Figure 4A,B), the plasma membrane lipids receded quickly from the hydrophilic face of the β-sheet, often already during the equilibration steps. In concert, water flowed into the space vacated by the lipids along the sheet. On the side of the receding membrane, phospholipid headgroups wrapped around the now open membrane edge to shield the otherwise exposed hydrophobic membrane core from water. Across the open edge, the intracellular and the extracellular membrane leaflets could exchange lipids.

On a much longer timescale in the simulations, the length of this open membrane edge shortened. First, the edge straightened by receding further from the interior of the pore; then, the open ends of the arc-shaped GSDMD^{NT} multimers were gradually pulled together.

In case of the 27-mer arc, this contraction resulted in the formation of a circular pore with a diameter of ≈17 nm within 4 μs (Figure 4B, Movie S2). By contrast, the 16-mer arc cracked at the center as the membrane edge shortened. After ≈0.9 μs, inter-subunit contacts between the globular domains of the middle subunits were lost, which resulted in the formation of a kink in the arc (Figure 4A, Movie S1). As the open ends of the two sub-arcs further contracted, a slit-shaped membrane pore formed. Importantly, despite the loss of contacts between the globular domains, the inserted β-sheet stayed fully intact, even in the highly curved kink region of the pore.

Membrane edge tension exerts large force on gasdermin arcs. We quantified the force acting on the open protein edges by determining the edge tension for our plasma membrane mimetic. From a simulation of a system without protein and with two plasma membrane edges that could not close under the condition of fixed box area, we determined the membrane edge tension per unit length of open edge as $\gamma = 86.4 \pm 3.9$ pN for our plasma membrane mimetic. This edge tension is the force exerted onto the ends of the gasdermin arcs once the edge has straightened. On a molecular scale, this force is large, amounting to a drop in free energy by 21 k_BT for a 1-nm edge shortening.

Gasdermin-D arc in DOPC membrane closes into circular pore. For reference, we also performed a simulation of a $GSDMD^{NT}$ 16-mer in a pure 1,2-dioleoyl-sn-glycero-3-phosphocholine (DOPC) membrane. For DOPC, a lower membrane edge tension of 44.3 ± 2.1[24] has been reported. Compared to the plasma membrane mimetic, the lipids receded more rapidly from the inserted β-barrel to form a pore (within 400 ns, Figure S2). As the membrane edge contracted, the $GSDMD^{NT}$ arc kinked in three positions to form a nearly circular pore rather than the slit-shaped pore seen in the plasma membrane mimetic.

Discussion

Shared lipid binding sites could promote oligomerization. Lipid interactions play an important role in the function of pore-forming proteins.[25] Xia et al.[3] identified three basic patches and with the help of mutational studies confirmed that they partake in the recognition of acidic lipid headgroups: the basic α1-helix (basic patch (BP) 1, "thumb"), the loop between β-strands 1 and 2 (β1-β2 loop, BP2, "wrist"), and two basic residues (R174, K204) of β-strands 7 and 8, respectively. In the MD simulations, we found that these basic patches do not act independently of each other. In particular, the flexible β1-β2 loop shares interaction sites with all of the other arginine and lysine rich sites. Further, we were able to specify several residues that we propose to fulfil key functions in $GSDMD^{NT}$ membrane binding.

In addition, our simulations revealed that $GSDMD^{NT}$ binds the plasma membrane differently, depending on whether it is in its monomeric prepore conformation or its oligomeric pore conformation. Differences in the strength of these interactions may drive the reorientation of $GSDMD^{NT}$ on the membrane during the transition from prepore to pore conformation. The described differences also point to certain residues involved in membrane binding, but not pore formation, such as K145, Q149, and R151. In variants with K145 and R151 mutated to alanine, oligomerization and pyroptosis are compromised, as is localization to the detergent phase in lysed cells.[18] Furthermore, while entropically unfavorable, binding of a single $PI(4,5)P_2$ to R7, R174, and R178 at the same time may kinetically trap these three residues in a distinct pore-like orientation long enough to facilitate the folding of the β-hairpin. This may also explain the preference of gasdermins to form pores in membranes containing multivalent acidic lipids such as $PI(4,5)P_2$, phosphatidylinositol-3,4,5-triphosphate ($PI(3,4,5)P_3$) and cardiolipin.[17]

Finally, we often observe one $PI(4,5)P_2$ bridging the interface of two neighboring subunits via their lateral binding sites. This suggests that during oligomerization, the acidic lipids bound to one side of one $GSDMD^{NT}$ subunit promote the addition of another $GSDMD^{NT}$

subunit, which binds the same acidic lipids via one of its lateral binding sites. Even if this "double-sided tape" may not confer high mechanical strength to the multimerization interface, it may facilitate oligomerization by attracting membrane-bound oligo- and monomers to the same location and by helping to orient them with respect to each other. It is therefore also interesting to see that the 33-mer in prepore conformation is even more interconnected by PI(4,5)P_2 than the 33-mer in pore conformation (Figure 1C). These lipid-mediated interactions should facilitate prepore assembly on the plasma membranes, which is rich in PI(4,5)P_2. Combined with our observation of joint binding sites within one subunit, this mechanism could provide an additional explanation for the preference of $GSDMD^{NT}$ for multivalent acidic lipids[17] and for the recent observation that it shows less diverse pore conformations in PI(4,5)P_2 or PI(3,4,5)P_3 rich membranes than in pure phosphatidylethanolamine (PE)/phosphatidylcholine (PC) membranes.[26]

Pores may grow by fusion of small membrane inserted segments. In earlier work, we found that the membrane β-sheet of monomeric pneumolysin was pushed out of the membrane within 1 μs in one of two atomistic replica simulations.[27] It was therefore surprising to us that the β-hairpins of monomeric and dimeric $GSDMD^{NT}$ stayed stably membrane inserted for the entirety of our 5 μs simulations. This opens up the possibility that $GSDMD^{NT}$ inserts its β-sheet already from such small oligomers, which then remain stably inserted and could diffuse together to form slit and ring-shaped pores. In addition, the fact that the pores formed by small oligomers already permit water and ion conduction across the membrane is perfectly in line with observed ion flux and size exclusion in the early phases of pyroptosis.[21–23] Sterically, release of IL-1 family cytokines[28,29] will require pores of at least 10 $GSDMD^{NT}$ subunits.

Furthermore, we occasionally found the interface between globular domains of neighboring subunits to break under stress. By contrast, the membrane inserted β-sheet always stayed intact, even in the highly curved kink region of slit-shaped pores. This remarkable

stability of the β-sheet and adaption to high curvature suggests that β-sheet formation may stabilize GSDMD^{NT} oligomers in pore conformation.

In AFM experiments, Mulvihill et al.[19] identified an abundance of membrane inserted slit-shaped pores. Recently, Santa Cruz Garcia et al.[26] discovered that GSDMD^{NT} pores may be able to dynamically open and close and they discuss that slit-shaped pores may provide the closed state to which open rings can collapse. With our 16-mer membrane inserted system, we identified a pathway that leads to the formation of pores similar in shape and size to these experimentally reported ones. We further show that slit-shaped pores can form spontaneously from arcs, driven by the tension along an open membrane edge.

Taken together, these results suggest that already monomers and small oligomers can support stable membrane insertion. Similar to the α pore-forming toxin ClyA, these smaller inserted oligomers may fuse with one another to build larger slit and finally ring-shaped pores.[30] This assembly, however, will happen on much longer timescales than currently accessible with atomistic MD simulations.

Lastly, the atomistic resolution of our simulations ensures a realistic flexibility of the protein assemblies, which allowed the open edge caused by β7 and β8 to partly rotate out of the membrane. As a result, one edge of the β-sheet is partly exposed. It would therefore provide an excellent attachment point for the β-strands of non-inserted subunits at the membrane surface, and may guide them towards the growing assembly and, eventually, into the membrane. In this way, the upward-tilt of one β-sheet edge would drive sequential oligomer growth along this edge.

Pore formation from prepore ring. From the above considerations, two competing assembly pathways emerge. High concentrations of prepore GSDMD^{NT} on the membrane would promote assembly into full prepore rings before folding and inserting the continuous β-sheet. The observed upward bending of the membrane into the prepore ring inside is consistent with a pull on the domain that has to unravel to form the membrane inserted β-

barrel. Similar to how antimicrobial peptides are believed to facilitate pore formation, locally confined adherence of many of the thus far unfolded hairpins would increase the membrane surface tension within the ring.[31] The resulting kink in the membrane at the inner edge of the prepore ring (Figures 2B and S1B) may facilitate the insertion of the β-strands. The instabilities we see in the globular domains of the circular prepore assembly are likely coupled to this strong membrane deformation.

Bilayer and solvent composition influence pore formation. The lipid composition has a crucial effect on the assembly of pore forming proteins on the membrane and the subsequent insertion of their pore opening components.[32] Higher membrane fluidity should lead to easier insertion of the membrane penetrating components and facilitate the formation of smaller pores. By contrast, increased lipid order should facilitate the formation of larger pores.

Here, we used a complex, asymmetric membrane composition mimicking the plasma membrane.[33] The high cholesterol content makes the membrane comparably stiff, which in turn leads to slower diffusion and higher tension of the open membrane edge. As such, it differs from typical lipid mixtures that are commonly used for microscopic experiments of GSDMD.[3,19,34] For these experimental model membranes, we expect edge tensions about half of that of our plasma membrane mimetic.[35] By simulating the 16-mer arc structure also in pure DOPC, we could illustrate the potential effect this can have: small pores form faster and are more circular than in the more rigid plasma membrane.

As further complications, the plasma membrane of eukaryotic cells interacts with the cytoskeleton and the bilayers used in AFM experiments are usually supported on a solid surface. Indeed, single particle tracking, spectroscopic measurements, and MD studies showed substantially lowered lipid diffusion between the directly supported and the unsupported leaflet.[36–39] We expect these interactions to impact the pore assembly pathways, in particular by lowering the membrane edge tension, an effect amplified by dissolved molecules

and proteins that preferentially bind to the open edge, and by slowing the dynamics in the membrane. How strong these effects can be is impressively highlighted by experimental observations of certain detergents lowering the membrane edge tension by up to two orders of magnitude and by the fact that lipids purchased from different suppliers yield drastically different strengths of the edge tension, presumably due to impurities.[40,41]

As an additional factor, arcs may be artificially stabilized on a crowded membrane by contacts to neighboring GSDMD^{NT} oligomers (e.g., by forming stacked or interlocking arcs). Together, these effects may explain the observation that arcs are quite abundant in experiments on GSDMD^{NT} and other beta pore forming proteins,[19,27,42–44] yet above a certain size do not remain stable in our simulations.

Differences between GSDMD and GSDMA3. A recent independent study of mouse GSDMA3 N-terminal domain (GSDMA3^{NT})[20] allows us to compare different gasdermins. In coarse-grained simulations, a 14-mer inserted GSDMA3^{NT} was found to break up and transition to a slit-like pore,[20] similar to what we observed here in atomistic MD simulations of a GSDMD^{NT} 16-mer. Also consistent with our findings for GSDMD^{NT}, GSDMA3^{NT} rings in pore conformation remained stable in atomistic MD simulations, whereas prepore rings proved comparably fragile and broke up.[20]

As a crucial difference to GSDMD^{NT}, the small GSDMA3^{NT} oligomer[20] did not form a membrane pore. Within 4 μs of atomistic MD, the membrane did not detach from the arc-shaped GSDMA3^{NT} 7-mer to form a membrane edge.[20] Missing the driving force for contraction, the arc remained stable without curling up. This is in stark contrast to our observations that water-filled and ion-conducting pores formed quickly for all oligomer sizes (Figure 3). As discussed above, the choice of membrane will likely impact the shape and stability of pores, and the missing sterols in the *E. coli* polar lipid extract[20] will have resulted in a less stiff membrane. However, a large difference in the hydrophilicity of the pore-facing residues is the most likely cause for the detachment of the lipid bilayer from GSDMD^{NT}

but not GSDMA3^{NT}. On the Eisenberg hydrophobicity scale,[45] the GSDMD^{NT} pore is 60% more hydrophilic than the GSDMA3 pore^{NT} (Table S2). Therefore, the difference between our results for GSDMD^{NT} oligomers and those for a GSDMA3^{NT} 7-mer[20] highlight how the physicochemical properties of the different gasdermins may be tuned to very specific membrane environments, cellular contexts or pore formation pathways. Based on the marked differences in hydrophilicity of the pore-facing side of the inserted β-sheets, it is tempting to speculate that—unlike GSDMA3^{NT}—GSDMD^{NT} allows the formation of sublytic pores that facilitate nonselective ion flux and thus dissipate the membrane potential, as seen in our simulations (Figure 3) and in experiment.[21–23]

Conclusions

In large-scale atomistic MD simulations we could resolve key steps in the formation of the large membrane pores by GSDMD^{NT}, as the ultimate effector of pyroptotic cell death.[1,2,5,6] The simulations give us a detailed view of the lipid interactions that target GSDMD^{NT} to the plasma membrane and that may trigger the change from the membrane-adhered prepore conformation to the membrane-inserted pore conformation. We also captured, in real time, the formation of membrane pores with diameters 1 to 20 nm, stabilized by oligomers up to 33 GSDMD^{NT}. The pores formed by small oligomers are stabilized by curled-up β-sheets. Small oligomers form arc-shaped pores that are water-filled and ion-conducting. Such pores can account for the early ion flux observed experimentally.[21–23] For larger GSDMD^{NT} arcs, we found that the high tension of the open membrane edge created by pore formation, exerted sufficient force either to crack the arcs at their center, resulting in sealed slit pores, or, for even larger arcs, to close them into ring shapes. Reassuringly, the arc pores, slit pores, and ring pores formed in the simulations have also been seen in experiment and coarse-grained simulations.[19,20,42,43] Remarkably, despite the cracks between the globular domains and the associated large deformations, the pore-lining β-sheets remained intact to maintain stable

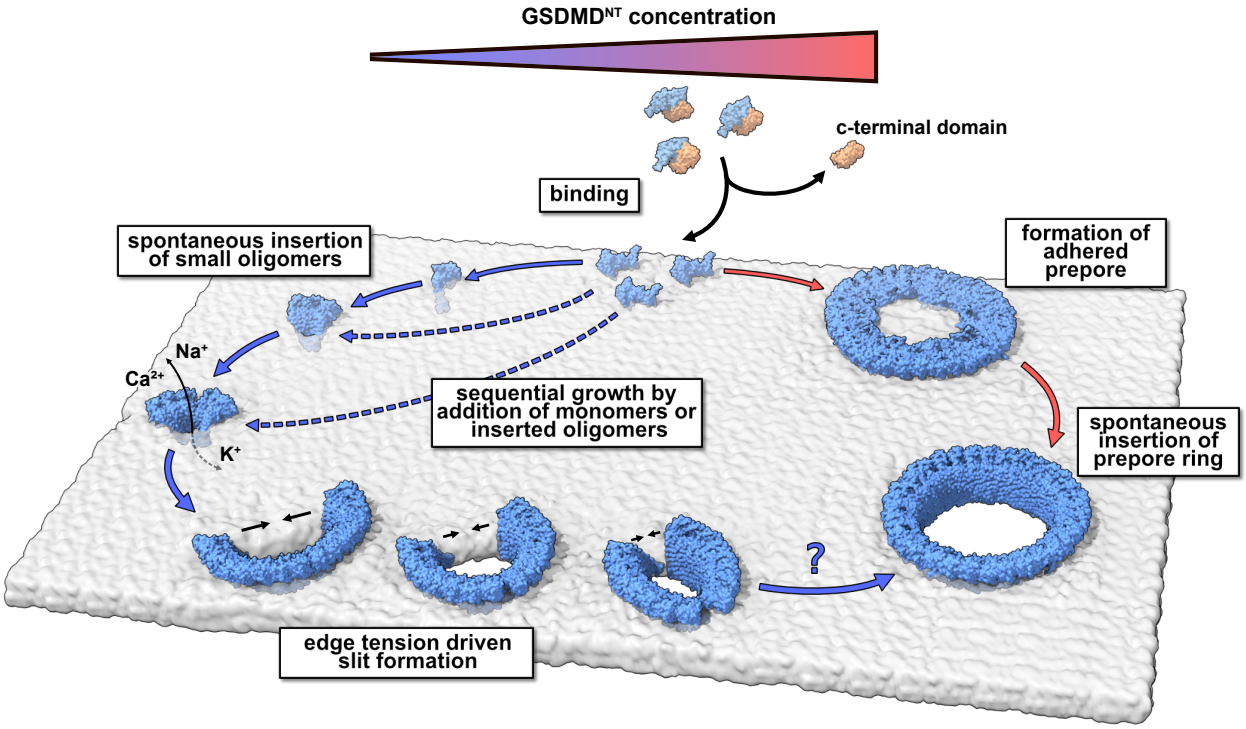

Figure 5: **Model of membrane pore formation by GSDMD^{NT}.** After proteolytic cleavage, GSDMD^{NT} monomers bind the inner leaflet of the plasma membrane. Aided by specific lipid interactions they multimerize and, at a critical size, spontaneously insert into the membrane. Depending on the concentration of membrane adhered GSDMD^{NT}, the insertion may proceed either from a fully formed prepore ring (clockwise) or from small oligomeric assemblies (counter-clockwise). Pores formed by small oligomers cause early nonspecific ion flux and can combine with one another or grow sequentially by the attachment of uninserted monomers. Depending on the edge tension in the cellular milieu, arcs would continue to grow or crack to form slit-shaped pores (bottom). Whether slit-shaped pores can grow to circular pores by subsequent monomer attachment is unclear.

membrane pores.

Our simulations suggest that GSDMD forms plasma membrane pores in two distinct pathways, as schematically illustrated in Figure 5. At low abundance of prepore GSDMD^{NT} on the membrane, we expect that small oligomers dominate. Eventual membrane insertion would then lead to small sublytic pores[21,23] (Figure 3) that could grow further by monomer addition and fusion. By contrast, high abundance of prepore GSDMD^{NT} on the membrane would tilt the kinetic balance towards the assembly of prepore rings and a collective β-sheet insertion. The formation of prepore rings would also be favored on membranes with

abundant PI(4,5)P_2 based on their preferential incorporation (Figure 1C).

Despite the detailed view of key steps in GSDMD-induced pore formation gained in our MD simulations, many important questions remain unanswered. In particular, the prepore-to-pore conformational transition and the insertion of the pore-lining β-sheet into the membrane have not yet been resolved. Our findings that prepore and pore conformations have distinct lipid interaction modes and that prepore rings pull the membrane upward into their center are suggestive as to possible drivers of the prepore-to-pore transition, but they do not yet address them directly. Similarly, the detailed assembly pathway of $GSDMD^{NT}$ on the membrane remains poorly understood. We found that small $GSDMD^{NT}$ oligomers in pore conformation present one edge of their β-sheets to the interface of the intracellular leaflet for the possible attachment of the unfolded β-strands of newly arriving monomers. Despite this suggestive finding, resolving the assembly and membrane insertion process will likely require a concerted effort that combines structural studies with dynamic imaging experiments and advanced MD simulations.

Materials and Methods

MD simulation parameters. All MD simulations were performed with GROMACS version 2020.3[46] using the CHARMM36m forcefield,[47] the TIP3P water model,[48] and an integration timestep of 2 fs. To calculate electrostatic interactions, we used the Particle Mesh Ewald (PME) algorithm.[49] Furthermore, we constrained the bond length of heavy atoms to hydrogens using the LINCS algorithm.[50]

During equilibration simulations in the NPT ensemble, a constant pressure was established with a semiisotropic Berendsen barostat[51] with the x and y dimensions of the simulation box coupled together. The reference pressure was 1 bar, the compressibility factor 4.5×10^{-5} bar^{-1}, and the barostat time constant 5 ps. A constant temperature of 37 $°C$ (310.15 K) was established with three separate Berendsen weak-coupling thermostats[51] ap-

plied to the protein, the solvent (including NaCl ions), and the membrane, each with a time constant of 1 ps.

The same general ensemble settings as for the equilibration simulations were used also for all production simulations. However, instead of the Berendsen weak-coupling algorithms we used the Parrinello-Rahman barostat for pressure control[52] and the velocity-rescale algorithm for temperature control.[53]

Membrane setup. To simulate $GSDMD^{NT}$ in its native environment, we designed a plasma membrane mimetic with asymmetric lipid composition. Following our earlier work[54] and Lorent et al.,[33] the outer leaflet of our membrane is rich in sphingolipids, phospholipids with PC headgroups and holds very few poly-unsaturated lipids. By contrast, the inner leaflet has a high content of lipids with PE headgroups and mostly polyunsaturated tails. In addition, the inner leaflet contains negatively charged $PI(4,5)P_2$ and PS lipids. Both leaflets were built with the same cholesterol concentration of 40 mol %.[33] The full composition is summarized in Table S1.

A small membrane patch with 99 lipids in the inner leaflet and 100 lipids in the outer leaflet, surrounded by water and 150 mM NaCl, was created using the Charmm-GUI membrane builder.[55,56] This membrane system was energy minimized using a steepest descent algorithm until the highest force acting on any atom fell below 1000 $kJ\,mol^{-1}$. The minimized system was then temperature and pressure equilibrated in six MD simulation steps with decreasing restraints on the phosphate headgroups and lipid tail dihedral angles (Table S3). Finally, the membrane was MD simulated for 5 µs at 70 $°C$ to promote cholesterol flip-flop that allows the membrane to equilibrate to tensionless leaflets.[57] After 3.5 µs no further net cholesterol flip-flop was observed and the resulting membrane patch was used to assemble all larger membranes used in this work.

Membrane edge tension simulation. To estimate the line tension of an open membrane edge of our plasma membrane composition, we removed a 9 nm wide strip of lipids from

a 20×20 nm^2 membrane patch in the xy plane. After resolvating the simulation box and deleting water molecules that were positioned between the membrane headgroup planes, this open membrane system was energy minimized and equilibrated for 5 ns (using parameters EM and Step 6 from Table S3). Following Jiang et al.,[58] between these two steps we rotated the entire system around the y-axis by 90 degrees to orientate the open membrane edge along z. This allowed us to fix the length of the box along z and therefore the length of the open edge, while pressure coupling the remaining two dimensions together. We then simulated the open membrane edge system for 530 ns. From this simulation, we then calculated the membrane edge tension γ by averaging the difference in lateral and normal pressures according to[58]

$$\gamma = \frac{1}{2}\left\langle L_x L_y \left[\frac{1}{2}(P_{xx} + P_{yy}) - P_{zz}\right]\right\rangle \tag{1}$$

with L_x and L_y being the fluctuating box dimensions in the x and y directions, respectively, and P_{xx}, P_{yy} and P_{zz} being the preset diagonal elements of the pressure tensor. The factor 1/2 accounts for the fact that we have two open membrane edges in our simulation system. Only the last 500 ns of the production run were considered for calculating the edge tension.

Pore conformation monomer and oligomer system setup. Using Charmm-GUI,[55,56] we extracted one monomer from the $GSDMD^{NT}$ structure in pore conformation (PDB Id 6VFE[3]), reversed the L192E mutation back to its native sequence and added capping groups to the termini to mimic the continuation of the peptide bond (acetylated N-terminus, amidated C-terminus). To build higher level multimers, we then copied the monomer as often as necessary and aligned it with the next respective subunit of the complete ring structure. In this way, we built $GSDMD^{NT}$ 2-mer, 3-mer, 5-mer, 8-mer, 10-mer, 16-mer, and 27-mer arcs, as well as a full ring consisting of 33 subunits.

The resulting monomer and the multimeric arc and ring structures were inserted into membranes created by replicating the previously described equilibrated membrane patch in the x and y directions. To remove clashes of overlaying lipid and protein atoms, all

lipid residues with at least one atom closer than 2 Å to any protein atom were removed. Additionally, lipids from within the pore were also removed in the case of the full ring system. To counteract the asymmetry introduced by removing different numbers of lipids from the outer and inner leaflet, we removed additional lipids from the leaflet containing excess lipids. We treated cholesterol molecules and all other phospholipids separately, and for each excess lipid of the respective group we removed a random lipid out of the leaflet holding more lipids.

Subsequently, all systems were solvated and ions were added. Due to the high negative charge of the membrane (in particular the inner leaflet) we introduced 150 mM of sodium ions to the system and then added excess chloride ions to neutralize the systems. All systems were then energy minimized as described above for the membrane system and subsequently equilibrated in three steps with varying restraints (Table S4). Note that unlike the equilibration of the membrane-only system, here lipid tail dihedral angles were never restrained, to allow for fast filling of space freed up by the removal of excess lipids. After equilibration, all systems were simulated without restraints and using the above described production simulation parameters for the simulation times summarized in Table S5.

Prepore conformation mono- and oligomer system setup. For setting up systems with $GSDMD^{NT}$ in prepore conformation, we took the back-mutated monomer that we used for the pore conformation simulations and manually bent its β-hairpins out of the membrane using the structure editing tool of PyMOL.[59] We then set up the simulation box setup and performed an energy minimization as for the systems in pore conformation. In the following 10 ns long equilibration run, only the positions of heavy protein atoms were restrained with force constants of 500 (backbone) and 100 (sidechains) $\mathrm{KJ\,mol^{-1}\,nm^{-2}}$, respectively.

Lipid binding site analysis. Using the PyLipID python library[60] and own code, we analyzed protein-lipid interactions for the prepore monomer and the full ring system in pore conformation. In particular, we characterized the interactions of the headgroup of $PI(4,5)P_2$ and PS lipids with the protein. Here, we disregarded the first 500 ns of the production

simulation and, from the remaining frames, collected all interactions where any headgroup atom came closer than 3.6 Å with respect to any protein residue. In case of the full 33-mer pore, we averaged lipid interactions over all 33 subunits. To minimize "rattling-in-a-cage" effects, we made use of the dual cutoff scheme suggested for PyLipID when analyzing the duration of these contacts. In this case, the duration of a lipid-protein contact was counted until the distance exceeded 5 Å. With this setup, assisted by visual analysis, we identified representative $PI(4,5)P_2$ binding sites.

Supporting Information Available

Supporting file (PDF) contains extended Tables S1-S5, Figures S1 and S2, and supporting movie legends for movies S1 and S2.

Acknowledgement

We thank Jürgen Köfinger, Hendrik Jung, Balázs Fábián, Shanlin Rao and Sergio Cruz-León for helpful discussions. This work was supported by the Clusterproject ENABLE funded by the Hessian Ministry for Science and the Arts.

References

(1) He, W. T.; Wan, H.; Hu, L.; Chen, P.; Wang, X.; Huang, Z.; Yang, Z. H.; Zhong, C. Q.; Han, J. Gasdermin D is an executor of pyroptosis and required for interleukin-1β secretion. *Cell Res.* **2015**, *25*, 1285–1298.

(2) Tsuchiya, K.; Hosojima, S.; Hara, H.; Kushiyama, H.; Mahib, M. R.; Kinoshita, T.; Suda, T. Gasdermin D mediates the maturation and release of IL-1α downstream of inflammasomes. *Cell Rep.* **2021**, *34*, 108887.

(3) Xia, S.; Zhang, Z.; Magupalli, V. G.; Pablo, J. L.; Dong, Y.; Vora, S. M.; Wang, L.; Fu, T.-M.; Jacobson, M. P.; Greka, A.; Lieberman, J.; Ruan, J.; Wu, H. Gasdermin D pore structure reveals preferential release of mature interleukin-1. *Nature* **2021**, *593*, 607–611.

(4) Xie, W. J.; Xia, S.; Warshel, A.; Wu, H. Electrostatic influence on IL-1 transport through the GSDMD pore. *Proc. Natl. Acad. Sci. U.S.A.* **2022**, *119*, 1–7.

(5) Shi, J.; Zhao, Y.; Wang, K.; Shi, X.; Wang, Y.; Huang, H.; Zhuang, Y.; Cai, T.; Wang, F.; Shao, F. Cleavage of GSDMD by inflammatory caspases determines pyroptotic cell death. *Nature* **2015**, *526*, 660–665.

(6) Kayagaki, N.; Stowe, I. B.; Lee, B. L.; O'Rourke, K.; Anderson, K.; Warming, S.; Cuellar, T.; Haley, B.; Roose-Girma, M.; Phung, Q. T.; Liu, P. S.; Lill, J. R.; Li, H.; Wu, J.; Kummerfeld, S.; Zhang, J.; Lee, W. P.; Snipas, S. J.; Salvesen, G. S.; Morris, L. X.; Fitzgerald, L.; Zhang, Y.; Bertram, E. M.; Goodnow, C. C.; Dixit, V. M. Caspase-11 cleaves gasdermin D for non-canonical inflammasome signalling. *Nature* **2015**, *526*, 666–671.

(7) Liu, X.; Xia, S.; Zhang, Z.; Wu, H.; Lieberman, J. Channelling inflammation: gasdermins in physiology and disease. *Nature Reviews Drug Discovery* **2021**, *20*, 384–405.

(8) Deng, W.; Bai, Y.; Deng, F.; Pan, Y.; Mei, S.; Zheng, Z.; Min, R.; Wu, Z.; Li, W.; Miao, R.; Zhang, Z.; Kupper, T. S.; Lieberman, J.; Liu, X. Streptococcal pyrogenic exotoxin B cleaves GSDMA and triggers pyroptosis. *Nature* **2022**, *602*, 496–502.

(9) Wen, W.; Li, X.; Wang, H.; Zhao, Q.; Yin, M.; Liu, W.; Chen, H.; Qian, P. Seneca valley virus 3c protease induces pyroptosis by directly cleaving porcine gasdermin D. *J. Immunol.* **2021**, *207*, 189–199.

(10) Peraro, M. D.; van der Goot, F. G. Pore-forming toxins: ancient, but never really out of fashion. *Nature Rev. Microbiol.* **2016**, *14*, 77–92.

(11) Ruan, J.; Xia, S.; Liu, X.; Lieberman, J.; Wu, H. Cryo-EM structure of the gasdermin A3 membrane pore. *Nature* **2018**, *557*, 62–67.

(12) Fink, S. L.; Cookson, B. T. Caspase-1-dependent pore formation during pyroptosis leads to osmotic lysis of infected host macrophages. *J. Immunol.* **2006**, *202*, 1913–1926.

(13) Wu, D.; Wei, C.; Li, Y.; Yang, X.; Zhou, S. Pyroptosis, a new breakthrough in cancer treatment. *Frontiers in Oncology* **2021**, *11*, 1–15.

(14) Ryder, C. B.; Kondolf, H. C.; O'Keefe, M. E.; Zhou, B.; Abbott, D. W. Chemical modulation of gasdermin-mediated pyroptosis and therapeutic potential. *J. Mol. Biol.* **2022**, *434*, 167183.

(15) Broz, P.; Pelegrín, P.; Shao, F. The gasdermins, a protein family executing cell death and inflammation. *Nature Rev. Immunol.* **2020**, *20*, 143–157.

(16) Aglietti, R. A.; Estevez, A.; Gupta, A.; Ramirez, M. G.; Liu, P. S.; Kayagaki, N.; Ciferri, C.; Dixit, V. M.; Dueber, E. C. GsdmD p30 elicited by caspase-11 during pyroptosis forms pores in membranes. *Proc. Natl. Acad. Sci. U.S.A.* **2016**, *113*, 7858–7863.

(17) Ding, J.; Wang, K.; Liu, W.; She, Y.; Sun, Q.; Shi, J.; Sun, H.; Wang, D. C.; Shao, F. Pore-forming activity and structural autoinhibition of the gasdermin family. *Nature* **2016**, *535*, 111–116.

(18) Liu, X.; Zhang, Z.; Ruan, J.; Pan, Y.; Magupalli, V. G.; Wu, H.; Lieberman, J. Inflammasome-activated gasdermin D causes pyroptosis by forming membrane pores. *Nature* **2016**, *535*, 153–158.

(19) Mulvihill, E.; Sborgi, L.; Mari, S. A.; Pfreundschuh, M.; Hiller, S.; Müller, D. J. Mechanism of membrane pore formation by human gasdermin-D. *EMBO J.* **2018**, *37*, 1–11.

(20) Mari, S. A.; Pluhackova, K.; Engel, A.; Müller, D. J.; Pipercevic, J.; Leipner, M. Gasdermin-A3 pore formation propagates along variable pathways. *Nature Commun.* **2022**, *13*, 1–14.

(21) de Vasconcelos, N. M.; Van Opdenbosch, N.; Van Gorp, H.; Parthoens, E.; Lamkanfi, M. Single-cell analysis of pyroptosis dynamics reveals conserved GSDMD-mediated subcellular events that precede plasma membrane rupture. *Cell Death and Differentiation* **2019**, *26*, 146–161.

(22) Chen, X.; He, W. T.; Hu, L.; Li, J.; Fang, Y.; Wang, X.; Xu, X.; Wang, Z.; Huang, K.; Han, J. Pyroptosis is driven by non-selective gasdermin-D pore and its morphology is different from MLKL channel-mediated necroptosis. *Cell Res.* **2016**, *26*, 1007–1020.

(23) Rühl, S.; Broz, P. Regulation of Lytic and Non-Lytic Functions of Gasdermin Pores. *J. Mol. Biol.* **2022**, *434*, 167246.

(24) West, A.; Ma, K.; Chung, J. L.; Kindt, J. T. Simulation studies of structure and edge tension of lipid bilayer edges: Effects of tail structure and force-field. *J. Phys. Chem. A* **2013**, *117*, 7114–7123.

(25) Hodel, A. W.; Rudd-Schmidt, J. A.; Trapani, J. A.; Voskoboinik, I.; Hoogenboom, B. W. Lipid specificity of the immune effector perforin. *Faraday Discuss.* **2021**, *232*, 236–255.

(26) Santa Cruz Garcia, A. B.; Schnur, K. P.; Malik, A. B.; Mo, G. C. Gasdermin D pores are dynamically regulated by local phosphoinositide circuitry. *Nature Commun.* **2022**, *13*, 1–11.

(27) Vögele, M.; Bhaskara, R. M.; Mulvihill, E.; van Pee, K.; Yildiz, Ö.; Kühlbrandt, W.; Müller, D. J.; Hummer, G. Membrane perforation by the pore-forming toxin pneumolysin. *Proc. Natl. Acad. Sci. U.S.A.* **2019**, *116*, 13352–13357.

(28) Kato, Z.; Jee, J. G.; Shikano, H.; Mishima, M.; Ohki, I.; Ohnishi, H.; Li, A.; Hashimoto, K.; Matsukuma, E.; Omoya, K.; Yamamoto, Y.; Yoneda, T.; Hara, T.; Kondo, N.; Shirakawa, M. The structure and binding mode of interleukin-18. *Nature Struct. Biol.* **2003**, *10*, 966–971.

(29) Finzel, B. C.; Clancy, L. L.; Holland, D. R.; Muchmore, S. W.; Watenpaugh, K. D.; Einspahr, H. M. Crystal structure of recombinant human interleukin-1β at 2·0 Å resolution. *J. Mol. Biol.* **1989**, *209*, 779–791.

(30) Benke, S.; Roderer, D.; Wunderlich, B.; Nettels, D.; Glockshuber, R.; Schuler, B. The assembly dynamics of the cytolytic pore toxin ClyA. *Nature Commun.* **2015**, *6*, 6198.

(31) Flores-Romero, H.; Ros, U.; Garcia-Saez, A. J. Pore formation in regulated cell death. *EMBO J.* **2020**, *39*, 1–18.

(32) Rojko, N.; Anderluh, G. How lipid membranes affect pore forming toxin activity. *Acc. Chem. Res.* **2015**, *48*, 3073–3079.

(33) Lorent, J. H.; Levental, K. R.; Ganesan, L.; Rivera-Longsworth, G.; Sezgin, E.; Doktorova, M.; Lyman, E.; Levental, I. Plasma membranes are asymmetric in lipid unsaturation, packing and protein shape. *Nat. Chem. Biol.* **2020**, *16*, 644–652.

(34) Hu, J. J.; Liu, X.; Xia, S.; Zhang, Z.; Zhang, Y.; Zhao, J.; Ruan, J.; Luo, X.; Lou, X.; Bai, Y.; Wang, J.; Hollingsworth, L. R.; Magupalli, V. G.; Zhao, L.; Luo, H. R.; Kim, J.; Lieberman, J.; Wu, H. FDA-approved disulfiram inhibits pyroptosis by blocking gasdermin D pore formation. *Nature Immunol.* **2020**, *21*, 736–745.

(35) Leomil, F. S. C.; Zoccoler, M.; Dimova, R.; Riske, K. A. PoET: automated approach for measuring pore edge tension in giant unilamellar vesicles. *Bioinf. Adv.* **2021**, *1*, 1–7.

(36) Schoch, R. L.; Barel, I.; Brown, F. L.; Haran, G. Lipid diffusion in the distal and prox-

imal leaflets of supported lipid bilayer membranes studied by single particle tracking. *J. Chem. Phys.* **2018**, *148*, 123333.

(37) Otosu, T.; Yamaguchi, S. Quantifying the diffusion of lipids in the proximal/distal leaflets of a supported lipid bilayer by two-dimensional fluorescence lifetime correlation spectroscopy. *J. Phys. Chem. B* **2018**, *122*, 10315–10319.

(38) Roark, M.; Feller, S. E. Structure and dynamics of a fluid phase bilayer on a solid support as observed by a molecular dynamics computer simulation. *Langmuir* **2008**, *24*, 12469–12473.

(39) Koutsioubas, A. Combined coarse-grained molecular dynamics and neutron reflectivity characterization of supported lipid membranes. *J. Phys. Chem. B* **2016**, *120*, 11474–11483.

(40) Karatekin, E.; Sandre, O.; Guitouni, H.; Borghi, N.; Puech, P. H.; Brochard-Wyart, F. Cascades of transient pores in giant vesicles: line tension and transport. *Biophys. J.* **2003**, *84*, 1734–1749.

(41) Puech, P. H.; Borghi, N.; Karatekin, E.; Brochard-Wyart, F. Line thermodynamics: adsorption at a membrane edge. *Phys. Rev. Lett.* **2003**, *90*, 4.

(42) Mulvihill, E.; Van Pee, K.; Mari, S. A.; Müller, D. J.; Yildiz, Ö. Directly observing the lipid-dependent self-assembly and pore-forming mechanism of the cytolytic toxin listeriolysin O. *Nano Lett.* **2015**, *15*, 6965–6973.

(43) Sborgi, L.; Rühl, S.; Mulvihill, E.; Pipercevic, J.; Heilig, R.; Stahlberg, H.; Farady, C. J.; Müller, D. J.; Broz, P.; Hiller, S. GSDMD membrane pore formation constitutes the mechanism of pyroptotic cell death . *EMBO J.* **2016**, *35*, 1766–1778.

(44) Leung, C.; Dudkina, N. V.; Lukoyanova, N.; Hodel, A. W.; Farabella, I.; Pandurangan, A. P.; Jahan, N.; Pires Damaso, M.; Osmanović, D.; Reboul, C. F.; Dun-

stone, M. A.; Andrew, P. W.; Lonnen, R.; Topf, M.; Saibil, H. R.; Hoogenboom, B. W. Stepwise visualization of membrane pore formation by suilysin, a bacterial cholesterol-dependent cytolysin. *eLife* **2014**, *3*, e04247.

(45) Eisenberg, D.; Weiss, R. M.; Terwilliger, T. C.; Wilcox, W. Hydrophobic moments and protein structure. *Faraday Symp. Chem Soc.* **1982**, *17*, 109–120.

(46) Abraham, M. J.; Murtola, T.; Schulz, R.; Páll, S.; Smith, J. C.; Hess, B.; Lindahl, E. GROMACS: High performance molecular simulations through multi-level parallelism from laptops to supercomputers. *SoftwareX* **2015**, *1-2*, 19–25.

(47) Huang, J.; Rauscher, S.; Nawrocki, G.; Ran, T.; Feig, M.; de Groot, B. L.; Grubmüller, H.; MacKerell, A. D. CHARMM36m: An improved force field for folded and intrinsically disordered proteins. *Nat. Methods* **2017**, *14*, 71–73.

(48) Jorgensen, W. L.; Chandrasekhar, J.; Madura, J. D.; Impey, R. W.; Klein, M. L. Comparison of simple potential functions for simulating liquid water. *J. Chem. Phys.* **1983**, *79*, 926–935.

(49) Essmann, U.; Perera, L.; Berkowitz, M. L.; Darden, T.; Lee, H.; Pedersen, L. G. A smooth particle mesh Ewald method. *J. Chem. Phys.* **1995**, *103*, 8577–8593.

(50) Hess, B.; Bekker, H.; Berendsen, H. J. C.; Fraaije, J. G. E. M. LINCS: A linear constraint solver for molecular simulations. *J. Comp. Chem.* **1997**, *18*, 1463–1472.

(51) Berendsen, H. J. C.; Postma, J. P. M.; van Gunsteren, W. F.; DiNola, A.; Haak, J. R. Molecular dynamics with coupling to an external bath. *J. Chem. Phys.* **1984**, *81*, 3684–3690.

(52) Parrinello, M.; Rahman, A. Polymorphic transitions in single crystals: A new molecular dynamics method. *J. Appl. Phys.* **1981**, *52*, 7182–7190.

(53) Bussi, G.; Donadio, D.; Parrinello, M. Canonical sampling through velocity rescaling. *J. Chem. Phys.* **2007**, *126*, 014101.

(54) Schaefer, S. L.; Jung, H.; Hummer, G. Binding of SARS-CoV-2 fusion peptide to host endosome and plasma membrane. *J. Phys. Chem. B* **2021**, *125*, 7732–7741.

(55) Jo, S.; Kim, T.; Im, W. Automated builder and database of protein/membrane complexes for molecular dynamics simulations. *PLoS One* **2007**, *2*, e880.

(56) Jo, S.; Kim, T.; Iyer, V. G.; Im, W. CHARMM-GUI: A web-based graphical user interface for CHARMM. *J. Comput. Chem.* **2008**, *29*, 1859–1865.

(57) Miettinen, M. S.; Lipowsky, R. Bilayer membranes with frequent flip-flops have tensionless leaflets. *Nano Lett.* **2019**, *19*, 5011–5016.

(58) Jiang, F. Y.; Bouret, Y.; Kindt, J. T. Molecular dynamics simulations of the lipid bilayer edge. *Biophys. J.* **2004**, *87*, 182–192.

(59) Schrödinger LLC, Warren DeLano, PyMOL. 2015; `http://www.pymol.org/pymol`.

(60) Song, W.; Corey, R. A.; Ansell, T. B.; Cassidy, C. K.; Horrell, M. R.; Duncan, A. L.; Stansfeld, P. J.; Sansom, M. S. P. PyLipID: A python package for analysis of protein–lipid interactions from molecular dynamics simulations. *J. Chem. Theory Comput.* **2022**, *18*, 1188–1201.